

PAPER

Robust and Accurate Ultrasound 3-D Imaging Algorithm Incorporating Adaptive Smoothing Techniques

Kenshi SAHO^{†a)}, *Student Member*, Tomoki KIMURA^{††}, *Nonmember*, Shouhei KIDERA^{†††}, Hirofumi TAKI[†], Takuya SAKAMOTO[†], *Members*, and Toru SATO[†], *Fellow*

SUMMARY Many researchers have proposed ultrasound imaging techniques for product inspection; however, most of these techniques are aimed at detecting the existence of flaws in products. The acquisition of an accurate three-dimensional image using ultrasound has the potential to be a useful product inspection tool. In this paper we apply the Envelope algorithm, which was originally proposed for accurate UWB (Ultra Wide-Band) radar imaging systems, to ultrasound imaging. We show that the Envelope algorithm results in image deterioration, because it is difficult for ultrasound measurements to achieve high signal to noise (S/N) ratio values as a result of a high level of noise and interference from the environment. To reduce errors, we propose two adaptive smoothing techniques that effectively stabilize the estimated image produced by the Envelope algorithm. An experimental study verifies that the proposed imaging algorithm has accurate 3-D imaging capability with a mean error of $6.1 \mu\text{m}$, where the transmit center frequency is 2.0 MHz and the S/N ratio is 23 dB. These results demonstrate the robustness of the proposed imaging algorithm compared with a conventional Envelope algorithm.

key words: *ultrasound 3-D imaging, accurate imaging, robust imaging, adaptive smoothing*

1. Introduction

An accurate three-dimensional (3-D) measurement method is essential in the production of devices with reflective surfaces. Although various optical 3-D imaging methods have been applied for this purpose [1], [2], the accuracy of these methods is degraded by the surface luminance of the objects under the test. Imaging methods based on ultrasound show promise, as they resolve most of the conventional issues. Although many ultrasound inspection methods have been proposed, [3]–[5] and have realized the accurate detection of cracks and their parameters, the images produced are two-dimensional (2-D), and not 3-D as required in our assumed application. Current 3-D imaging methods, such as the time-reversal [6], [7] and synthetic aperture methods, [8], [9], are not sufficiently accurate.

To resolve these problems, we apply an advanced algorithm developed for UWB (Ultra Wide-Band) radar systems

to our ultrasound system. A similar study has been reported in [10], in which the Shape Estimation Algorithm based on the Boundary Scattering Transform and Extraction of Directly scattered waves (SEABED) was applied to ultrasound data. SEABED is based on the reversible Boundary Scattering Transform (BST) between the time delay and target boundary [11], [12]. Although the algorithm was originally designed for Ultra Wide-Band (UWB) radar applications, it has been confirmed that SEABED can also be used to produce accurate 2-D acoustic images in cases with high S/N ratios [10]. This algorithm is, however, quite sensitive to small range errors, since the BST uses a derivative of the observed ranges.

To avoid this problem, we make use of another accurate 3-D imaging algorithm, the Envelope algorithm [13]. This method produces more accurate and stable images than the conventional SEABED algorithm. In the case of an extremely low S/N ratio, however, the image quality of this algorithm also deteriorates. This paper proposes two adaptive smoothing techniques that can be incorporated into the Envelope algorithm to improve its stability in a noisy environment. We propose a new method to stabilize the quasi-wavefront by adaptively selecting the more suitable smoothing technique. In the proposed quasi-wavefront smoothing method, false images caused by impulsive errors are removed by reference to the estimated signal power. Numerical simulations verify that the proposed imaging algorithm produces accurate images even for data with low S/N ratios.

The numerical analysis is followed by an experimental investigation with acoustic devices. The results of this experimental evaluation show that the proposed imaging algorithm works well even with noisy experimental data, by sustaining $6.1 \mu\text{m}$ accuracy for ultrasound pulses with a $700 \mu\text{m}$ pulsewidth.

2. Conventional Imaging Algorithm

2.1 System Model

Figure 1 shows the system model in which the target has an arbitrary convex shape with a boundary. An omnidirectional transmit/receive element is scanned on the plane. A wide-band pulse is transmitted from the element, which receives echoes through the same element. $s'(X, Y, t)$ is the signal received at $(x, y, z) = (X, Y, 0)$. Applying the matched filter to $s'(X, Y, t)$, we obtain $s(X, Y, Z')$ as the output of the

Manuscript received February 2, 2011.

Manuscript revised July 19, 2011.

[†]The authors are with the Department of Communications and Computer Engineering, Graduate School of Informatics, Kyoto University, Kyoto-shi, 606-8501 Japan.

^{††}The author is with the Medical Equipment Group, Canon, Tokyo, 146-8501 Japan.

^{†††}The author is with the Graduate School of Informatics and Engineering, the University of Electro-Communications, Chofu-shi, 182-8585 Japan.

a) E-mail: k.saho@e06.mbox.media.kyoto-u.ac.jp

DOI: 10.1587/transcom.E95.B.572

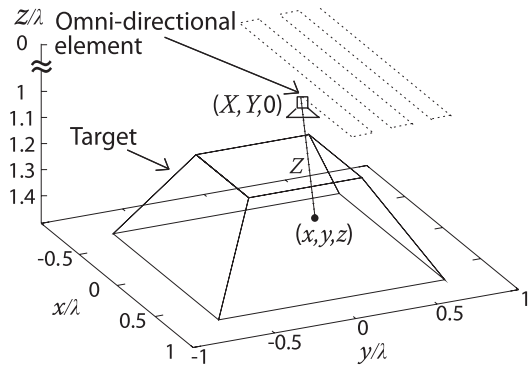


Fig. 1 System model.

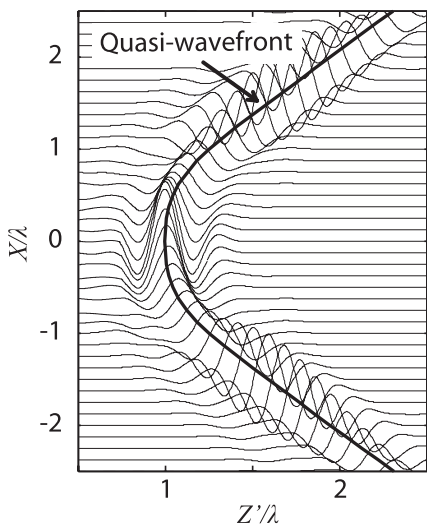


Fig. 2 Example of received signals and a quasi-wavefront with $Y = 0$.

filter, where $Z' = vt/2$ is expressed by time t and the speed of the wave v . The significant peaks of $s(X, Y, Z')$ are connected to produce a function $Z(X, Y)$ and surface (X, Y, Z) , called a quasi-wavefront, where Z is the peak along the Z' axis of $s(X, Y, Z')$. We do not consider the effect of multipaths because this paper assumes a convex target. Figure 2 shows an example of received signals as $s(X, Y, Z')$ and a quasi-wavefront with $Y = 0$. The transform from (X, Y, Z) to (x, y, z) corresponds to the imaging that is our focus in this paper.

2.2 Envelope Algorithm

The Envelope algorithm is based on the principle that an arbitrary target boundary can be expressed as an outer or inner envelope of spheres [13]. Each sphere has its center at $(X, Y, 0)$ and radius Z . Figure 3 shows the relationship between the target boundary and an envelope of circles, and refers to a 2-D problem for simplicity. For a convex target, the z -coordinate of the boundary can be calculated for each (x, y) as

$$z = \max_{X,Y} \sqrt{Z^2 - (x - X)^2 - (y - Y)^2}. \tag{1}$$

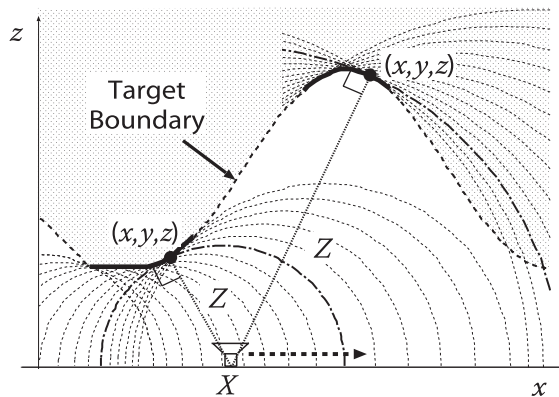


Fig. 3 Relationship between target boundary and envelopes of circles in a 2-D monostatic problem.

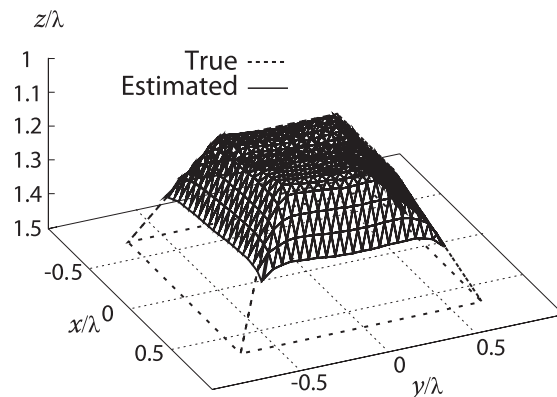


Fig. 4 Estimated image using the Envelope algorithm with $S/N=32$ dB.

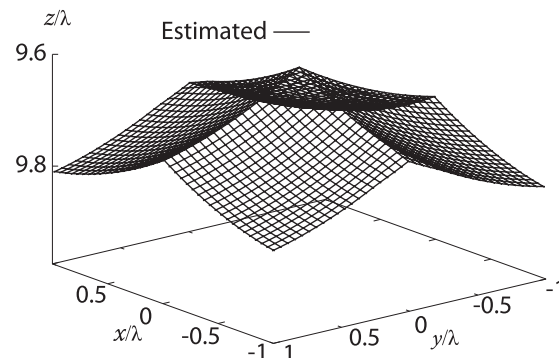


Fig. 5 Estimated image using the Envelope algorithm with $S/N=21$ dB.

2.3 Noise Tolerance of Envelope Algorithm

In this section, we investigate the performance of the Envelope algorithm in a noisy environment through numerical simulation. This simulation employs a frustum of a pyramid as the target, as shown in Fig. 1. In our tests, the transmitting pulse is a monocycle pulse with a center frequency of 2.0 MHz, a bandwidth of 1.2 MHz, and a wavelength λ of $746 \mu\text{m}$. We scan an element with co-ordinates $-1.732\lambda < X < 1.732\lambda, -1.732\lambda < Y < 1.732\lambda$, and then

transmit pulses and receive echoes at 41×41 locations. White noise is added to the received signals calculated using the Physical Optics (PO) method [14]–[17]. Figures 4 and 5 show the images estimated using the Envelope algorithm with S/N=32 dB and 21 dB, respectively, where the S/N ratio is defined as the peak value of the $s(X, Y, Z')$ to the effective value of the noise. Although the estimated image is quite accurate when S/N=32 dB, severe degradation is seen on the image when S/N=21 dB. This is because the Envelope method calculates the maximum Z for each (x, y) .

3. Proposed Adaptive Smoothing Techniques

In this section, two new techniques are proposed to enhance the noise tolerance of the conventional Envelope algorithm. The proposed imaging algorithm is the Envelope algorithm incorporating these proposed smoothing techniques. These techniques are characterized by their adaptive smoothing processes, which depend on the S/N ratio of the data. The proposed adaptive smoothing techniques comprises the following two processes:

1. Quasi-wavefront smoothing
2. False image reduction

Figure 6 shows the procedure for the proposed imaging algorithm including these techniques. The proposed adaptive smoothing techniques are examined in the following subsections.

3.1 Quasi-Wavefront Smoothing Method

A random error of a quasi-wavefront is transformed to a non-negligible distortion of the image produced by the Envelope algorithm. Figure 7 illustrates how the image is distorted by an impulse error in the range estimate. As shown in this figure, the estimated image can be masked by an incorrect circle, even if only one range estimate has an error. This type of large error can be suppressed by re-estimating the range that is detected as an anomaly after the first estimate. The proposed smoothing method also employs a Gaussian filter and a conditional median filter [18], and selects their smoothing process adaptively.

The procedure for re-estimating the improper points (REIP) is presented below.

- Step 1). Find an incorrect point Z_n that satisfies $(\partial Z/\partial X)^2 + (\partial Z/\partial Y)^2 > 1$ and $S/N > \alpha$. If $S/N \leq \alpha$, we remove this point.
- Step 2). Calculate the median value, Z_m , from the ranges Z of 8 adjacent elements around Z_n .
- Step 3). Update Z by finding the peak value of $s(X, Y, Z)$ around $Z_m \pm \lambda$.

This re-estimation process suppresses large range errors. However, non-negligible errors remain on the quasi-wavefront after the re-estimation. To suppress these errors, a conditional median filter (CMF) [18] is used. This filter is known to be suitable for smoothing non-stationary signals, such as the quasi-wavefront. The CMF calculates the me-

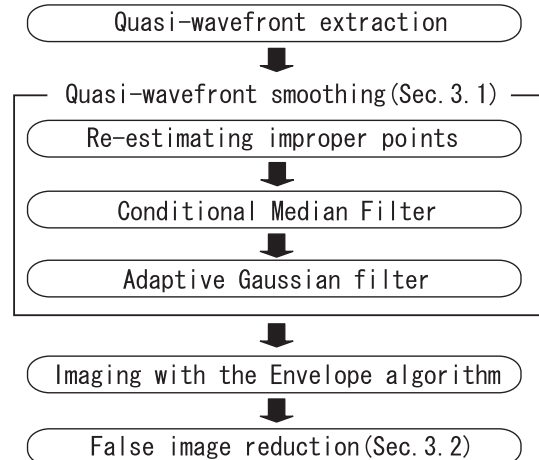


Fig. 6 Procedure for proposed imaging algorithm.

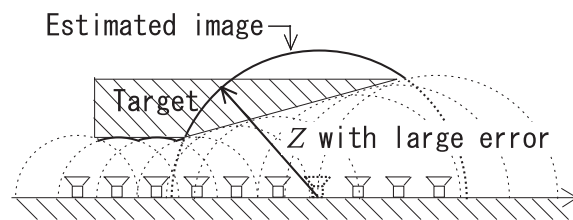


Fig. 7 Example showing the estimation of a large error in a 2-D problem.

dian Z_{cm} from the $N \times N$ data, whose center is the input data Z . The output data of the CMF is calculated as

$$Z_o = \begin{cases} Z & (|Z - Z_{cm}| < \beta) \\ Z_{cm} & (\text{Otherwise}). \end{cases} \quad (2)$$

If $|Z - Z_{cm}|$ is smaller than the threshold β , we regard Z as a large erroneous point, and the CMF suppresses these types of errors using Eq. (2).

However, the CMF cannot smooth small range errors. To suppress these residual range errors, an adaptive Gaussian smoothing technique (AGS) [10] is used. This technique is suitable for suppressing small errors in the quasi-wavefront. The AGS uses the Gaussian filter with an optimum correlation length, which is approximated as

$$\sigma = \sqrt{\frac{\delta_{\max} Z}{\pi}}, \quad (3)$$

where δ_{\max} is the limit value of the distortion on the quasi-wavefront caused by the Gaussian filter. This equation means that the AGS selects the correlation length depending on the smoothness of the quasi-wavefront. If the quasi-wavefront is sufficiently smooth, σ is set to a large value to enhance noise tolerance. If not, the AGS sets σ to a small value to avoid deterioration in accuracy.

Thus, the proposed quasi-wavefront smoothing method selects the smoothing process of these filters depending on the property of the quasi-wavefront, and achieves an improvement in both robustness and accuracy.

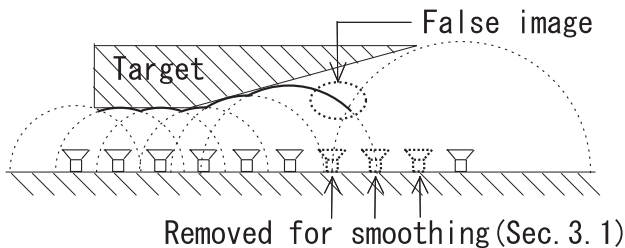


Fig. 8 Example showing the false image yielded by 2-D monostatic problem.

3.2 False Image Reduction

Figure 8 illustrates the false image produced by the Envelope method at one end of the image. As shown in this figure, the false image is expressed as part of the circle at the end. Because some data are removed in the first step of the process described in the previous section, the vacant area is naturally interpolated with a pair of circles by the Envelope method, causing this type of false image. To remove this false image, an evaluation value ϕ_i is introduced as

$$\phi_i = \begin{cases} \max_{Z'} s(X_i, Y_i, Z')^2 / (A_i / Z_i) & (A_i \neq 0) \\ 0 & (A_i = 0), \end{cases} \quad (4)$$

where A_i is the estimated area of part of the sphere for (X_i, Y_i, Z_i) . Using this evaluation value means that we can effectively remove the large image area estimated from a low-power echo. Moreover, this evaluation value does not depend on the position of the elements, thus we can remove false images in all locations. The procedure for the false image reduction method follows. We calculate ϕ_i for each element location as $(X_i, Y_i, 0)$. We set the threshold of the evaluation level ϕ_{th} , and remove the spheres if $\phi_i < \phi_{th}$ is satisfied.

4. Performance Evaluation with Numerical Simulations

4.1 The Performance of the Envelope Algorithm Improved by the Smoothing Methods

This section evaluates the accuracy and noise tolerance of the proposed imaging algorithm, which combines the Envelope algorithm and the various smoothing methods described in the previous section. The transmitting pulse, the element location, and the target are the same as in Sect. 2.3. To clarify the effectiveness of each adaptive smoothing technique, we add the techniques to the Envelope algorithm one by one, and evaluate the accuracy of the estimated image for each. We evaluate the accuracy of each method quantitatively, using the evaluation value μ_{max} defined as

$$\mu_{max} = \max_i \sqrt{\min_{\mathbf{x}} \|\mathbf{x} - \mathbf{x}_e^i\|^2}, \quad (5)$$

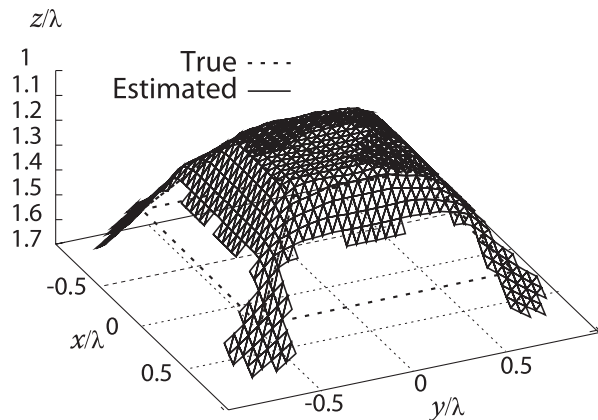


Fig. 9 Image estimated using the quasi-wavefront smoothing (Sect. 3.1) and the Envelope algorithm with S/N=21 dB.

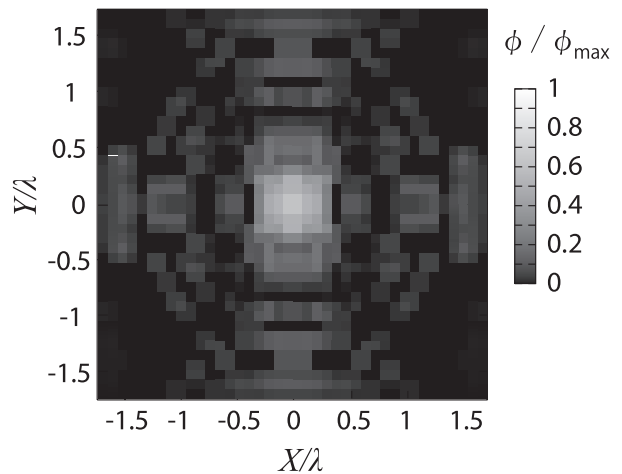


Fig. 10 Evaluation value ϕ for each antenna location.

where \mathbf{x} and \mathbf{x}_e^i denote the locations of the true target point and the estimated point.

First, we incorporate quasi-wavefront smoothing method (Sect. 3.1) with the Envelope algorithm. Figure 9 shows the resulting estimated image with S/N=21 dB. Parameters of the coordinates are normalized by λ . We set $N = 3$, $\alpha = 8.5$ dB, $\beta = 0.1\lambda$, and $\delta_{max} = 0.1\lambda$. As shown in this figure, an accurate image is estimated using the smoothing method apart from the false images at the ends. This is because the power of signals received from the edge of the target is relatively small. The accuracy μ_{max} is $2.13 \times 10^{-1}\lambda$, which is relatively large due to the false image.

Next, we apply the false image reduction method (Sect. 3.2) to the data in Fig. 9. Figure 10 shows the evaluation level ϕ_i normalized by the maximum value of each element location. As shown in this figure, ϕ_i at the side of the scanning range is relatively small, and these ϕ_i correspond to the false images. In this case, we set the threshold $\phi_{th} = 0.05\phi_{max}$, where ϕ_{max} is the maximum value of ϕ_i . Figure 11 shows the estimated image with the proposed imaging algorithm in which false images are correctly removed. Here, μ_{max} is $1.15 \times 10^{-2}\lambda$. These results verify that

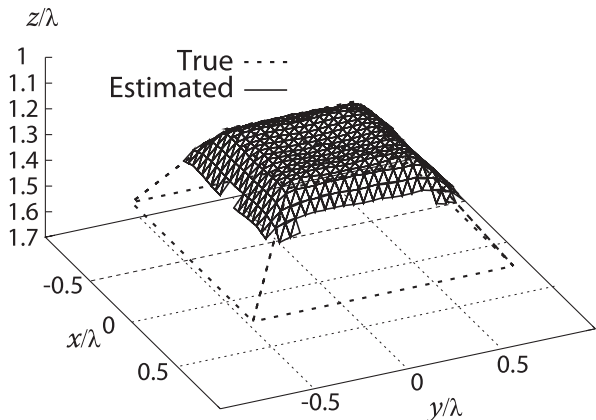


Fig. 11 Image estimated using the proposed imaging algorithm (Sects. 3.1 and 3.2 and the Envelope) with $S/N=21$ dB.

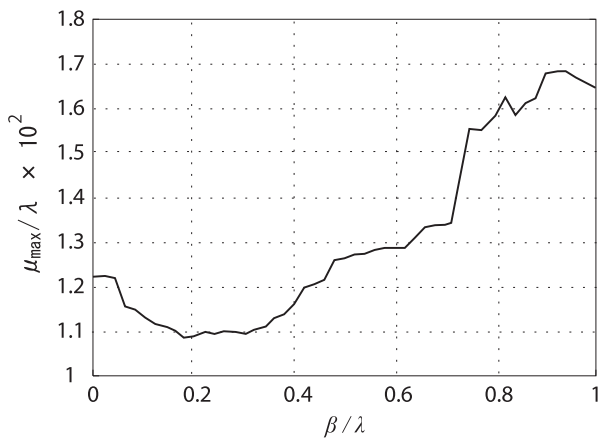


Fig. 12 Relationship between μ_{\max} and β with $S/N=20$ dB.

the proposed imaging algorithm realizes accurate imaging even for lower S/N ratio values.

4.2 Evaluation of Suitable Parameters and Noise Tolerance

This section discusses the properties of the proposed imaging algorithm for various cases. First, we investigate the suitable parameters for the CMF: the threshold β and filter size N . Figure 12 shows the relationship between β and μ_{\max} , and Table 1 shows μ_{\max} for each N and β , where the S/N is 20 dB. These results indicate that the estimation of accurate images is not sensitive to the parameter values. In this example, although μ_{\max} becomes relatively small in $0.05\lambda < \beta < 0.4\lambda$, sufficiently accurate imaging is realized when $\beta < 0.7\lambda$. In addition, Table 1 indicates that the suitable N is 3 for all β . However, μ_{\max} is $1.37 \times 10^{-2}\lambda$ and less when $N \leq 7$ and $\beta \leq 0.3\lambda$. Therefore, we can easily choose appropriate parameters to perform a few examples for each condition. To verify the validity of the above discussion, we show another shape estimation example. Here we assume a square pyramid target. Based on the above discussion, we set $\beta = 0.2\lambda$ and $N = 3$. Other parameters are the same as in

Table 1 μ_{\max} for each N and β ($\times 10^{-2}\lambda$).

β/λ	N	3	5	7
0.1		1.16	1.23	1.23
0.2		1.10	1.21	1.28
0.3		1.10	1.25	1.37

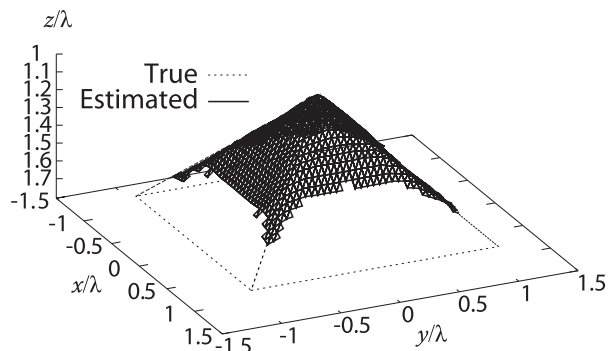


Fig. 13 Estimated image of a square pyramid target ($\beta = 0.2\lambda$, $N = 3$, and $S/N=20$ dB).

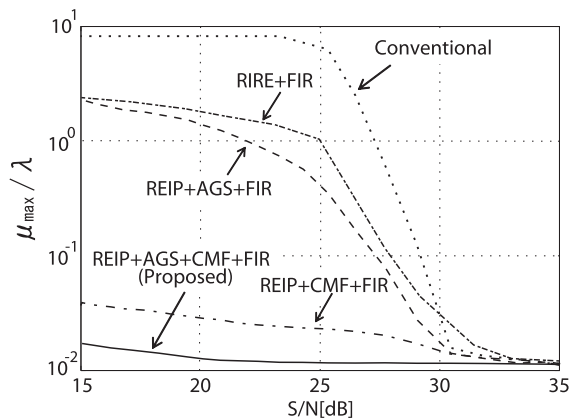


Fig. 14 Relationship between μ_{\max} and the S/N ratio for each smoothing filter.

the previous section. Figure 13 shows the estimated image with a $S/N=20$ dB. This figure shows that accurate imaging is also realized in this case. μ_{\max} is $1.18 \times 10^{-2}\lambda$. This result indicates that the proposed imaging algorithm realizes accurate imaging for a variety of convex targets when the parameters are set appropriately.

Next, we clarify the noise tolerance for each quasi-wavefront smoothing method. We assume that the target is the same as in the previous section. Figure 14 shows the relationship between the S/N and μ_{\max} for each filter. Here, the false image reduction method (FIR) is used in cases without the conventional algorithm. This figure shows that the accuracy of the conventional algorithm deteriorates when the $S/N < 30$ dB. In the cases using the REIP and AGS without the CMF, although the noise tolerance improved slightly, the accuracy of these cases also deteriorated for $S/N < 28$ dB. This is due to the relatively large residual errors. On the other hand, using the CMF, we can suppress these large er-

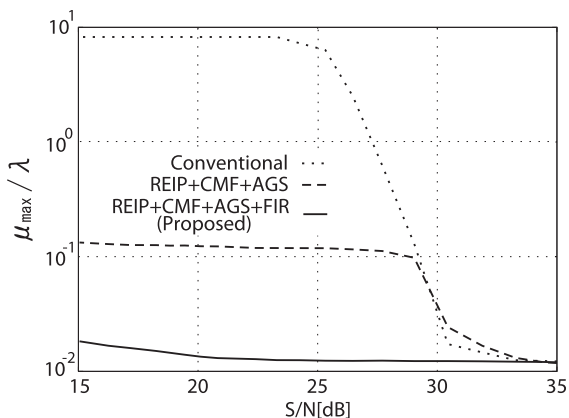


Fig. 15 Relationship between μ_{\max} and the S/N ratio for each technique.

rors, and estimate an accurate image even for data with low S/N ratios. Furthermore, the proposed imaging algorithm achieves more accurate imaging using both the AGS and CMF, because the AGS suppresses other small errors left by the CMF.

Finally, we show the effectiveness of the FIR and the synergy of the adaptive smoothing techniques. Figure 15 shows the relationship between μ_{\max} and the S/N ratio for each method described in Sect. 3. As indicated in this figure, by applying quasi-wavefront smoothing (Sect. 3.1), the accuracy improved 100-fold. By applying both methods (Sects. 3.1 and 3.2), the accuracy is further improved 10-fold. These results clarify the synergy of the proposed techniques. In particular, the accuracy of the proposed imaging algorithm is $\mu_{\max} < 1.5 \times 10^{-2} \lambda$ when the S/N > 18 dB.

5. Experiments for Accurate Ultrasound Imaging

In this section, we investigate the performance of the proposed imaging algorithm experimentally and present our results.

5.1 Experimental Setup

Figure 16 illustrates the experimental setup with a transducer and a needle hydrophone as transmitting and receiving elements. Figure 17 shows the vertical section of the scanning plane for the sensor and target location. The separation between the transducer and needle hydrophone is 13.21 mm in the y-direction. The center of the measuring unit is scanned in the range $0 \leq X \leq 25$ and $0 \leq Y \leq 25$ mm, with a sampling interval of 1 mm. A stainless steel spherical target, 3.17 mm in diameter, is placed in the water, with the scanning plane and target 61.7 mm apart. A transducer transmits acoustic pulses with a center frequency of 2.0 MHz and a -6 dB fractional bandwidth of 0.6. The aperture size of the transducer is 13 mm, and the transducer is designed to focus at a depth of 25.4 mm. The transmit beam behind the focal point is approximately a spherical wave with a broad beam width of 46 degrees. Figure 18 shows a received signal with $(X, Y) = (0, 0)$. The S/N ratio is approximately 23 dB. The

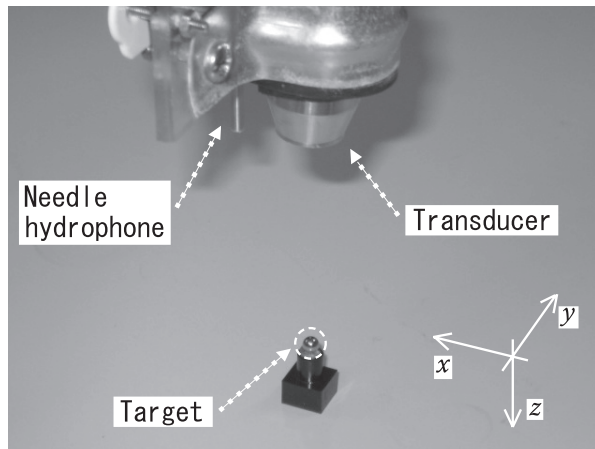


Fig. 16 Instruments utilized in the acoustic imaging experiment.

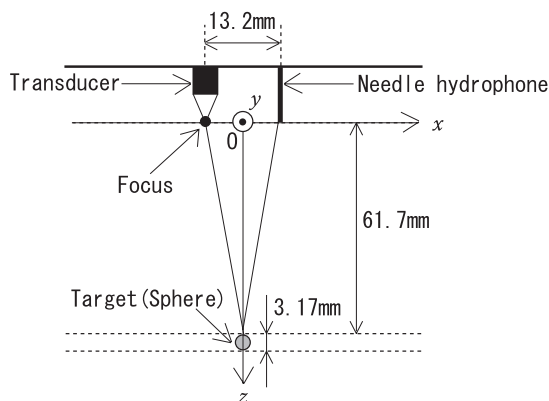


Fig. 17 Vertical section of the scanning plane for the sensor and target location.

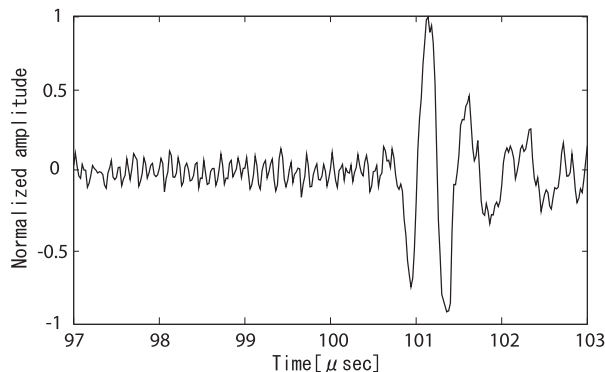


Fig. 18 Example of received signal.

amplitude of the transmitted signal is amplified to 40 Vpp by a power amplifier, before entering the transducer. The needle hydrophone receives echoes from the target, and a digital oscilloscope samples the pre-amplified signals received. The sampled signals are coherently averaged 10,000 times. The speed of the ultrasound is 1492.2 m/s, calculated in water temperature of 23.5°C [19], and the wavelength λ is approximately 746 μm . The procedure for the proposed imag-

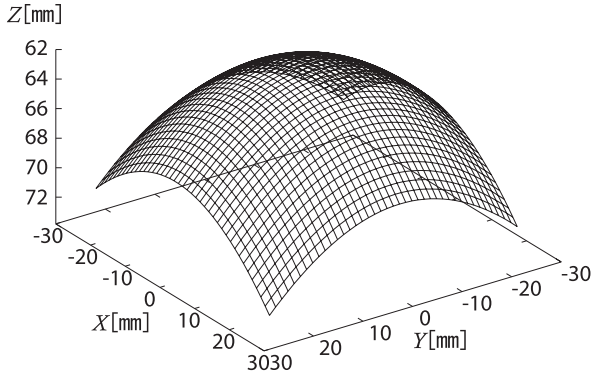


Fig. 19 True quasi-wavefront.

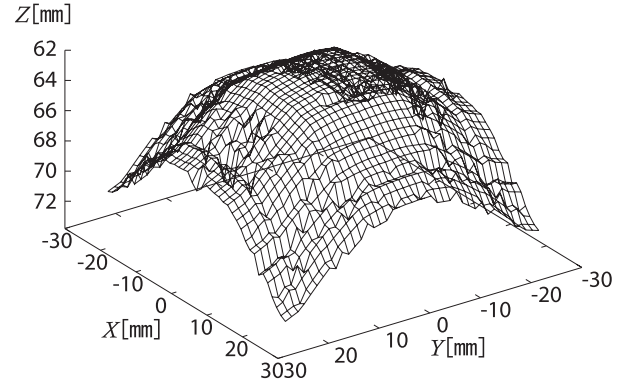


Fig. 20 Quasi-wavefront extracted from the received signals.

ing algorithm is the same as for the numerical simulations described in the previous section.

5.2 Modified Imaging Algorithm for Experimental Data

In this experiment, we use the bi-static sensor layout shown in Fig. 17. In the experiment for the ultrasound system, we confirmed that the range finding accuracy is not distorted when using the bi-static system [10]. Moreover, we have already achieved accurate imaging with the bi-static UWB radar system [13]. Consequently, we employed the bi-static system for ultrasound imaging. In a bi-static model, the target boundary is estimated from the envelope of ellipsoids with focal points on the location of the transducer and needle hydrophone. The value of z is calculated for each (x, y) as

$$z(x, y) = \max_{X, Y} \sqrt{Z^2 - d^2 - (y - Y)^2 - \frac{(Z^2 - d^2)(x - X)^2}{Z^2}}. \quad (6)$$

where the separation between the transmitting and receiving elements is defined as $2d$, and $(X, Y, 0)$ is the center point of the two elements.

5.3 Performance of the Proposed Imaging Techniques with Experimental Data

The actual quasi-wavefront calculated by the BST [11], and the estimated quasi-wavefront, are shown in Figs. 19 and 20. It can be seen that the quasi-wavefront includes many large errors, especially around the side of the scanning area. This is due to the false peak estimate of $s(X, Y, Z)$. Figure 21 shows the image estimated by applying the Envelope algorithm to the quasi-wavefront in Fig. 20, and the vertical section of the actual and estimated images for $x = 0$. Figure 21 shows that the estimated image is not accurate, because inaccurate signals, caused by noise, mask other image surfaces. The range-finding accuracy in this experiment, of the order of μm , is not sufficient to determine the location of the true target. Thus, we translate the estimated image to the correct location by minimizing the RMS value of the difference between the actual target and the estimated images.

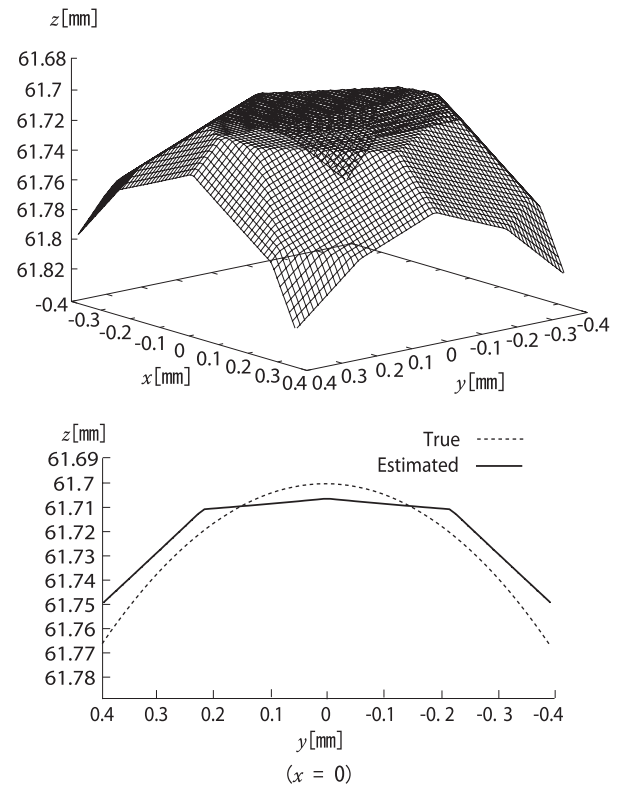


Fig. 21 Estimated image without the adaptive smoothing techniques (above) and the vertical section of the estimated image and target with $x=0$ (below).

Figure 22 shows the quasi-wavefront, after applying the proposed adaptive smoothing techniques. We empirically set $N = 3$, $\alpha = 7.0 \text{ dB}$, $\beta = 100 \mu\text{m}$, and $\delta_{\text{max}} = 90 \mu\text{m}$. This confirms that the proposed adaptive smoothing techniques can remove large errors on the quasi-wavefront. The image estimated by the proposed imaging algorithm and the vertical section of the estimated image and target for $x = 0$ are depicted in Fig. 23. Since the Envelope algorithm employs wide transmit and receive beams, a single transmit and receive event only reveals that the target boundary borders an ellipse. However, the algorithm depicts the target boundary using the outer envelope of ellipses calculated from mul-

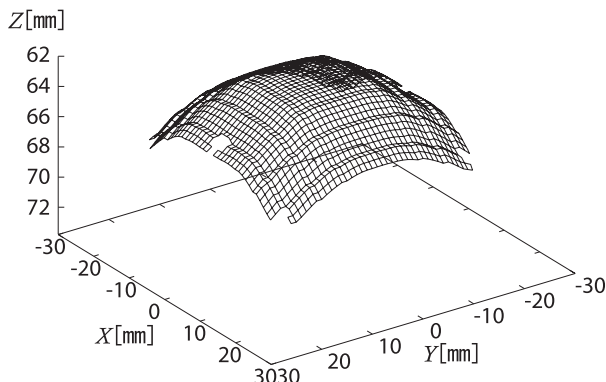


Fig. 22 Estimated quasi-wavefront using the adaptive smoothing techniques.

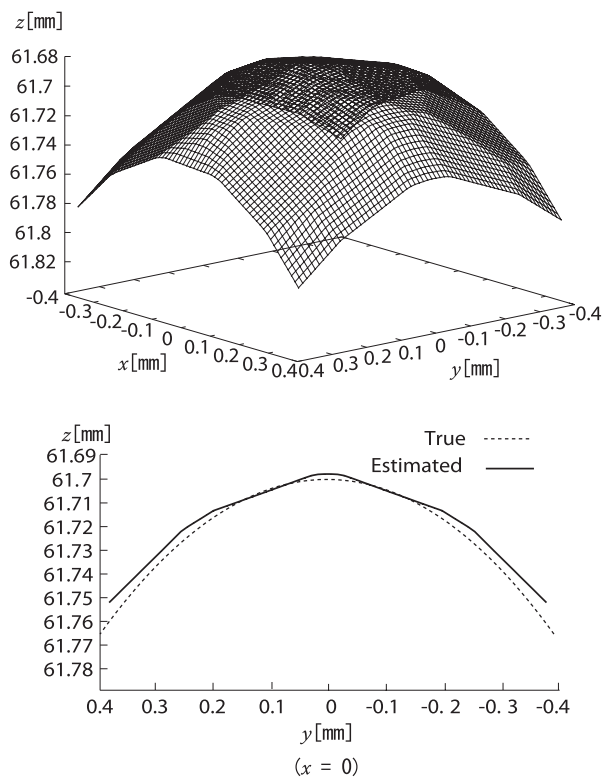


Fig. 23 Image estimated using the adaptive smoothing techniques (above) and the vertical section of the estimated image and target with $x=0$ (below).

multiple transmit and receive events. The experimental study shows that the Envelope algorithm works properly in ultrasound imaging. In addition, the proposed adaptive smoothing techniques improve the robustness of the Envelope algorithm, and an accurate 3-D image was acquired for a $S/N = 23$ dB, where the performance of a conventional Envelope algorithm deteriorates severely for a $S/N < 28$ dB. The mean error is $6.1 \mu\text{m}$ which corresponds to $8.2 \times 10^{-3} \lambda$.

6. Conclusions

In this paper we have proposed a 3-D ultrasound imaging

algorithm with adaptive smoothing techniques. Accurate imaging is achieved even with a low S/N ratio. The results from numerical simulations show that the maximum error of the estimated image is less than $1.5 \times 10^{-2} \lambda$ when the $S/N > 18$ dB. We have also applied the proposed imaging algorithm to 3-D acoustic measurement data, and evaluated the performance of this algorithm experimentally. This investigation verified that the proposed imaging algorithm also achieves accurate imaging for ultrasound data. The mean error of the estimated image is $6.1 \mu\text{m}$, which corresponds to 8.2×10^{-3} for $S/N = 23$ dB, confirming that the proposed imaging algorithm can realize robust and accurate 3-D acoustic imaging in a real environment.

Acknowledgments

This work is partly supported by the Innovative Techno-Hub for Integrated Medical Bio-imaging Project of the Special Coordination Funds for Promoting Science and Technology from the Ministry of Education, Culture, Sports, Science and Technology (MEXT), Japan.

References

- [1] Y. Tang, X. Su, F. Wu, and Y. Liu, "A novel phase measuring deflectometry for aspheric mirror test," *Opt. Express*, no.17, vol.ww, pp.19778–19784, 2009.
- [2] T. Morimoto, M. Matsui, M. Fujigaki, and A. Matsui, "Three-dimensional displacement analysis by windowed phase-shifting digital holographic interferometry," *Strain*, vol.44, no.1, pp.49–56, 2008.
- [3] J. Zhang, B.W. Drinkwater, P.D. Wilcox, and A.J. Hunter, "Defect detection using ultrasonic arrays: The multi-mode total focusing method," *NDT & E International*, vol.43, no.2, pp.123–133, 2010.
- [4] S. Wagle and H. Kato, "Ultrasonic wave intensity reflected from fretting fatigue cracks at bolt joints of aluminum alloy plates," *NDT & E International*, vol.42, no.8, pp.690–695, 2009.
- [5] J. Westlund, "2D SH modelling of ultrasonic testing for cracks near a non-planar surface," *Eng. Anal. Bound. Elem.*, vol.33, no.8-9, pp.1103–1112, 2009.
- [6] N. Dominguez and V. Gibiat, "Non-destructive imaging using the time domain topological energy method," *Ultrasonics*, vol.50, no.3, pp.367–372, 2010.
- [7] S.G. Conti, P. Roux, and W.A. Kuperman, "Near-field time-reversal amplification," *J. Acoust. Soc. Am.*, vol.121, no.6, pp.3602–3606, 2007.
- [8] A.J. Hunter, B.N. Drinkwater, and P.D. Wilcox, "The wavenumber algorithm for full-matrix imaging using an ultrasonic array," *IEEE Trans. Ultra. Ferro. Freq. Contr.*, vol.55, no.11, pp.2450–2462, 2008.
- [9] S. Repetto, M. Palmese, and A. Trucco, "High-resolution 3-D imaging by a sparse array: Array optimization and image simulation," *Oceans-Europe 2005*, vol.2, pp.763–768, 2005.
- [10] T. Sakamoto, T. Kimura, H. Taki, and T. Sato, "An experimental study on a fast imaging method with reversible transform for ultrasonic short pulse," *Proc. IEICE Gen. Conf. 2008*, A-11-8, March 2008 (in Japanese).
- [11] T. Sakamoto and T. Sato, "A target shape estimation algorithm for pulse radar systems based on boundary scattering transform," *IEICE Trans. Commun.*, vol.E87-B, no.5, pp.1357–1365, May 2004.
- [12] T. Sakamoto, S. Kidera, T. Sato, and S. Sugino, "An experimental study on a fast 3-D imaging algorithm for UWB pulse radars," *IEICE Trans. Commun. (Japanese Edition)*, vol.J90-B, no.1, pp.66–73, Jan. 2007.

- [13] S. Kidera, T. Sakamoto, and T. Sato, "High-resolution and real-time 3-D imaging algorithm with envelope of spheres for UWB radars," *IEEE Trans. Geosci. Remote Sens.*, vol.46, no.11, pp.3503–3513, 2008.
- [14] Y.Z. Umul, "Modified theory of physical optics," *Opt. Express*, vol.12, no.20, pp.4959–4971, 2004.
- [15] H. Taki and T. Sato, "High-resolution real-time three-dimensional acoustic imaging system with a reflector," *J. Med. Ultrasonics*, vol.34, pp.133–144, 2007.
- [16] H. Taki and T. Sato, "Improved spatial resolution in a three-dimensional acoustic medical imaging system based on a hybrid method using a synthetic aperture technique," *Jpn. J. Appl. Phys.*, vol.46, no.7B, pp.4827–4833, 2007.
- [17] Y. Dong, P.R. Runkle, L. Carin, R. Damarla, A. Sullivan, M.A. Ressler, and J. Sichina, "Multi-aspect detection of surface and shallow-buried unexploded ordnance via ultra-wideband synthetic aperture radar," *IEEE Trans. Geosci. Remote Sens.*, vol.39, no.6, pp.1259–1270, 2001.
- [18] T. Kasparis, M. Georgiopoulos, and E. Payne, "Non-linear filtering techniques for narrow-band interference rejection in direct sequence spread-spectrum systems," *Proc. IEEE Mil. Commun. Conf.*, vol.1, pp.360–364, 1991.
- [19] K.V. Mackenzie, "Discussion of sea-water sound-speed determinations," *J. Acoust. Soc. Am.*, vol.70, no.3, pp.801–806, 1981.



Kenshi Saho received his B.E. degree from Kyoto University in 2008 and M.I. degree from Graduate School of Informatics, Kyoto University in 2010. He is currently studying for a Ph.D. degree at Graduate School of Informatics, Kyoto University. His research interest is in signal processing for remote sensing.



Tomoki Kimura received the B.E. degree in Electrical and Electronic Engineering from Kyoto University in 2007 and the M.I. degree in Informatics from Kyoto University in 2009. Then he joined Canon Inc., and has been engaged in the development of software for medical equipment.



Shouhei Kidera received his B.E. degree in Electrical and Electronic Engineering from Kyoto University in 2003 and M.I. and Ph.D. degrees in Informatics from Kyoto University in 2005 and 2007, respectively. He is an assistant professor in Graduate School of Informatics and Engineering, University of Electro-Communications, Japan. His current research interest is in advanced signal processing for the near field radar, UWB radar. He is an associate member of the Institute of Electrical and Electronics Engineering (IEEE) and a member of the Institute of Electrical Engineering of Japan (IEEJ).



ber.

Hirofumi Taki received a M.D. degree from Kyoto University in 2000, a Ph.D. degree in informatics from Kyoto University in 2007, and is presently a research staff at Kyoto University. He has worked on development of the spatial resolution and calcification detection ability in Ultrasonography. IEEE, Japan Society of Ultrasonics in Medicine, Acoustic Society of Japan, The Institute of Electronics, Information and Communication Engineers, Japan Society for Medical and Biological Engineering mem-



Takuya Sakamoto received his B.E. degree from Kyoto University in 2000, and M.I. and Ph.D. degrees from the Graduate School of Informatics, Kyoto University in 2002 and 2005, respectively. He is an assistant professor in the Department of Communications and Computer Engineering, Graduate School of Informatics, Kyoto University. His current research interest is in UWB radar signal processing. He is a member of the IEEJ and the IEEE.



Toru Sato received his B.E., M.E., and Ph.D. degrees in electrical engineering from Kyoto University, Kyoto, Japan in 1976, 1978, and 1982, respectively. He has been with Kyoto University since 1983 and is currently a Professor in the Department of Communications and Computer Engineering, Graduate School of Informatics. His major research interests include system design and signal processing aspects of UWB radars, atmospheric radars, radar remote sensing of the atmosphere, and radar observation of space debris. He is a member of the Institute of Electrical and Electronics Engineers, the Society of Geomagnetism and Earth, Planetary and Space Sciences, the Japan Society for Aeronautical and Space Sciences, and American Meteorological Society.